Atomistic simulation study of short pulse laser interactions with a metal target under conditions of spatial confinement by a transparent overlayer

Eaman T. Karim,[1] Maxim Shugaev,[1] Chengping Wu,[1] Zhibin Lin,[2] Robert F. Hainsey,[2] and Leonid V. Zhigilei[1,a)]
[1]*Department of Materials Science and Engineering, University of Virginia, 395 McCormick Road, Charlottesville, Virginia 22904-4745, USA*
[2]*Electro Scientific Industries, Inc., 13900 NW Science Park Drive, Portland, Oregon 97229, USA*

(Received 28 February 2014; accepted 7 April 2014; published online 8 May 2014)

The distinct characteristics of short pulse laser interactions with a metal target under conditions of spatial confinement by a solid transparent overlayer are investigated in a series of atomistic simulations. The simulations are performed with a computational model combining classical molecular dynamics (MD) technique with a continuum description of the laser excitation, electron-phonon equilibration, and electronic heat transfer based on two-temperature model (TTM). Two methods for incorporation of the description of a transparent overlayer into the TTM-MD model are designed and parameterized for Ag-silica system. The material response to the laser energy deposition is studied for a range of laser fluences that, in the absence of the transparent overlayer, covers the regimes of melting and resolidification, photomechanical spallation, and phase explosion of the overheated surface region. In contrast to the irradiation in vacuum, the spatial confinement by the overlayer facilitates generation of sustained high-temperature and high-pressure conditions near the metal-overlayer interface, suppresses the generation of unloading tensile wave, decreases the maximum depth of melting, and prevents the spallation and explosive disintegration of the surface region of the metal target. At high laser fluences, when the laser excitation brings the surface region of the metal target to supercritical conditions, the confinement prevents the expansion and phase decomposition characteristic for the vacuum conditions leading to a gradual cooling of the hot compressed supercritical fluid down to the liquid phase and eventual solidification. The target modification in this case is limited to the generation of crystal defects and the detachment of the metal target from the overlayer. © *2014 AIP Publishing LLC*.
[http://dx.doi.org/10.1063/1.4872245]

I. INTRODUCTION

While the general mechanisms of short pulse laser melting, spallation, and ablation of metals in vacuum and in a background gas have been extensively studied experimentally, theoretically, and computationally, the effect of strong spatial confinement of the laser-induced processes by a solid transparent overlayer remains largely unexplored. The spatial confinement is realized when a metal target (a film or a bulk substrate) is covered by a transparent overlayer and the laser irradiation is focused on the metal surface through the overlayer. This setup has been shown to be advantageous for a number of practical applications, from laser shock peening[1–4] to laser-induced forward transfer[5–7] and thin film patterning/scribing,[8,9] and to the generation of high-quality surface nanostructures.[10] In particular, a substantial increase in pressure generated in laser ablation confined by a glass overlayer[1,2,11] has been utilized in material processing by laser-induced shock waves[1–4] and has enabled design of "exotic targets" with enhanced momentum transfer for laser propulsion applications.[12] Recently, the generation of periodic nanostructures by multiple beam interference has been reported for Ni and Si surfaces covered by optically transparent 400 nm thick polymer layers.[10] A significant improvement in the quality of the nanostructured surfaces, as compared to processing of bare surfaces, is observed and attributed to the suppression of the expansion and breakup of molten material as well as trapping of the ejected droplets by the overlayer.

The analytical description and computer modeling of laser-induced processes under conditions of spatial confinement have been largely focused on thermodynamic analysis of the evolution of pressure exerted on the metal target by the vapor/plasma plume expansion and evaluation of the momentum transfer to the irradiated target.[2,9,11,12] In several recent numerical simulations of thin film removal by back-side femtosecond pulse irradiation through a transparent substrate, the dynamics of the relaxation of thermo-elastic stresses and the mechanical deformation of the metal film are considered[4,13,14] and found to play the dominant role in the separation and ejection of the film fragments at laser fluences close to the ablation threshold.[13] The analysis of the effect of the spatial confinement on the kinetics and mechanisms of laser-induced phase transformation, as well as the structural modification of the metal target, however, is beyond the capabilities of the continuum-level finite difference[14] or finite element method[4,13] calculations. On the other hand, the atomistic molecular dynamics (MD) simulations, while more computationally expensive, have been shown to

a)Author to whom correspondence should be addressed. E-mail: lz2n@virginia.edu

be capable of providing detailed information on the fast non-equilibrium structural and phase transformations induced by short pulse laser irradiation of thin films[15–21] and bulk targets[21–29] under vacuum conditions or in the presence of background gas.[30]

In this paper, we report the results of the first MD simulations aimed at investigation of the mechanisms and kinetics of rapid laser-induced phase transformations in a bulk metal target covered by a thick transparent overlayer. The combined atomistic-continuum model accounting for the laser excitation, electron-phonon equilibration, and electronic heat transfer in the metal target, as well as two new methods for incorporation of the description of a transparent overlayer into the model, is described in Sec. II. The results of the simulations of laser interactions with a Ag target covered by a silica glass overlayer are reported and contrasted with the results observed for the same irradiation conditions in the absence of the confining overlayer in Sec. III. A brief summary of the results and a discussion of future research directions are provided in Sec. IV.

II. COMPUTATIONAL MODEL

The computational setups used in the simulations of laser interactions with a bulk Ag target covered by a transparent overlayer are schematically illustrated in Fig. 1. Two main components of the computational setup, the model for simulation of laser interaction with the metal target and the representation of the transparent overlayer, are described below.

A. TTM-MD model for Ag target

The laser interaction with the bulk Ag target is simulated with a model that combines the classical MD method with the two-temperature model (TTM)[31] that describes the evolution of lattice and electron temperatures by two coupled nonlinear differential equations and accounts for the laser excitation of the conduction band electrons, electron-phonon energy exchange, and electron heat conduction. In the combined TTM-MD model, MD substitutes the TTM equation for the lattice temperature, and the diffusion equation for the electron temperature is solved simultaneously with MD integration of the equations of motion of atoms. The cells introduced to solve the TTM equation for the electron temperature are related to the corresponding regions of the MD system. The local lattice temperature is then defined for each cell from the average kinetic energy of thermal motion of atoms. A complete description of the TTM-MD model is given in Ref. 32 and below we only delineate the computational setup and provide the parameters of the model used in the simulations reported in this paper.

The interatomic interactions in the Ag target are described by the embedded atom method (EAM) potential in the form proposed by Foiles, Baskes, and Daw (FBD).[33] A cut-off function[34] is added to the potential to smoothly bring the interaction energies and forces to zero at interatomic distance of 5.5 Å. Although the FBD EAM potential is fitted to low-temperature values of the equilibrium lattice constant, sublimation energy, bulk modulus, elastic constants, and vacancy formation energy, it also provides a good description of high-temperature thermodynamic properties of Ag relevant to the conditions of laser-induced melting and ablation. In

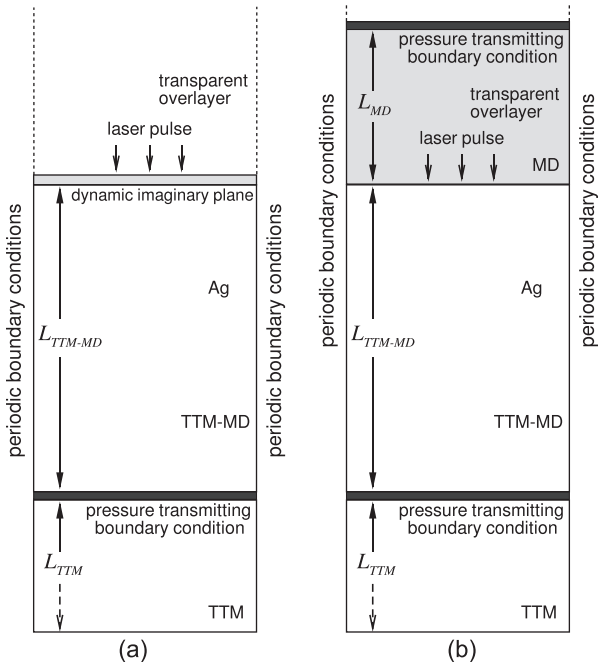

FIG. 1. Schematic sketches of two alternative computational setups designed for simulations of laser interaction with a Ag target covered by a transparent overlayer. In both setups, the top layer of the Ag target with thickness of L_{TTM-MD} is represented by the atomistic TTM-MD model, whereas the heat conduction in the deeper part of the substrate is simulated with TTM equations solved in the region with thickness of L_{TTM}. The transparent overlayer is represented by a dynamic imaginary plane in (a) and by a model adopting an atomistic MD description of a part of the overlayer adjacent to the Ag target in (b). The dynamic pressure-transmitting boundary conditions are applied at the bottom of the TTM-MD region and, in (b), at the top of the MD part of the overlayer to mimic non-reflective propagation of laser-induced pressure waves through the boundaries. In both setups, the partial propagation of the laser-induced pressure wave into the silica overlayer and the work of adhesion between the overlayer and the Ag target are reproduced.

particular, the equilibrium melting temperature, T_m, determined in liquid-crystal coexistence MD simulations is 1139 K,[35] about 8% below the experimental value of 1235 K.[36] The temperature and pressure conditions for the onset of the explosive phase separation into liquid and vapor, T^* and P^*, are determined for the FBD EAM Ag in a series of constant-pressure MD simulations of a slow (0.1 K/ps) heating of a metastable liquid, following an approach applied earlier to other material systems.[27,28,37,38] The onset of the phase explosion is identified from a sharp increase in volume of the system and the threshold temperature for the phase explosion is found to be about 3450 K at zero pressure and about 4850 K at 0.5 GPa. The onset of the phase explosion can be expected at ~10% below the critical temperature[38–40] and the values of T^* calculated for the FBD EAM Ag material are not in conflict with the broad range of experimental values of the critical temperature of Ag spanning from 4300 K to 7500 K.[41] At negative values of pressure, the onset of cavitation in the metastable liquid is observed at about 2060 K at −0.5 GPa, 1530 K at −1 GPa, and 1400 K at −1.5 GPa.

The choice of the parameters of the TTM equation for the electron temperature of Ag is the same as in Ref. 35, where a more detailed explanation of the parameters is provided. The electron temperature dependences of the electron-phonon coupling factor and electron heat capacity are taken

in the forms that account for the thermal excitation from the electron states below the Fermi level.[42] The temperature dependence of the electron thermal conductivity is described by the Drude model relationship, with parameters evaluated based on the free electron model and the experimental value of the thermal conductivity of Ag.[35]

The irradiation of the target with a 10 ps laser pulse is represented through a source term added to the TTM equation for the electron temperature.[32] The source term simulates excitation of the conduction band electrons by a laser pulse with a Gaussian temporal profile and reproduces the exponential attenuation of laser intensity with depth under the surface. To account for the energy transport occurring before the thermalization of the excited electrons, the optical absorption depth, $L_p = 12$ nm at laser wavelength of 1 μm,[43] is combined with the effective depth of the "ballistic" energy transport, $L_b = 56$ nm, roughly estimated here as a product of the Fermi velocity and the Drude relaxation time.[44] To ensure complete deposition of the energy of the 10 ps laser pulses, the peak intensity of the Gaussian laser pulse is shifted to 25 ps from the beginning of the simulations. The absorbed laser fluence, F_{abs}, rather than the incident fluence is used in the discussion of the simulation results.

As illustrated in Fig. 1, the atomic-level TTM-MD representation is used only for the top part of the Ag target, where the laser-induced structural modifications take place. The systems with different depth of the TTM-MD region, L_{TTM-MD}, are used at different laser fluences, namely, $L_{TTM-MD} = 209$ nm for $F_{abs} = 900\,\mathrm{J/m^2}$ and $F_{abs} = 1000\,\mathrm{J/m^2}$, $L_{TTM-MD} = 411$ nm for $F_{abs} = 3000\,\mathrm{J/m^2}$, and $L_{TTM-MD} = 699$ nm for $F_{abs} = 6000\,\mathrm{J/m^2}$. The heat transfer in the deeper part of the target is described by the TTM equations for lattice and electron temperatures solved down to the depth of $L_{TTM-MD} + L_{TTM}$, with $L_{TTM} = 2.5\mu$m chosen to ensure the absence of any significant increase in the electron or lattice temperatures at the bottom of the computational domain by the end of the simulation.

The lateral (parallel to the surface of the Ag target or the interface with the overlayer) dimensions of the computational systems are 4.1×4.1 nm^2, and the number of Ag atoms in the TTM-MD parts of the systems is 203 600 for $L_{TTM-MD} = 209$ nm, 399 600 for $L_{TTM-MD} = 411$ nm, and 680 000 for $L_{TTM-MD} = 699$ nm. The periodic boundary conditions are imposed in the lateral directions to reproduce the interaction of the atoms with the surrounding material. This approach is appropriate when the laser spot diameter is much larger than the depth of the laser energy deposition, so that any effects related to the lateral variations of the irradiation and thermal conditions can be neglected and the simulated part of the system remains laterally confined by the surrounding material during the time of the simulation. At the bottom of the TTM-MD part of the model, a special pressure-transmitting,[45,46] heat-conducting boundary condition is applied in order to avoid an artificial reflection of the laser-induced pressure wave and to account for the heat transfer from the surface region of the metal target, represented with atomic-level resolution, to the deeper part of the target, represented at the continuum level. The simulations are performed for systems with free metal surfaces exposed to the laser irradiation as well as for metal targets covered by thick transparent overlayers. The computational representation of the overlayer is described next.

B. Computational representation of the transparent overlayer

Two different methods developed in this work for representation of the transparent overlayer are illustrated in Fig. 1. In both implementations, the properties of fused silica are used in parameterization, and the overlayer is assumed to be sufficiently thick to ensure that the pressure wave generated in the overlayer due to the laser energy absorption by the metal target does not reflect from the top surface of the overlayer and come back to the metal-overlayer interface during the time of the simulation. For a 10 μm thick overlayer and the speed of sound of 5900 m/s in fused silica,[36] it takes more than 3 ns for the reflected wave to reach the interface. In the irradiation regimes considered in this work (from the threshold for surface melting up to several times the threshold), the time scale of laser-induced structural and phase transformations does not exceed several nanoseconds and the reflected pressure wave would not affect the transformations for overlayers with thickness on the order of tens of micrometers.

In the first method, illustrated in Fig. 1(a), the overlayer is not represented with atomic resolution but introduced through a dynamic acoustic impedance matching boundary condition that accounts for the displacement of the metal-overlayer interface in response to the thermal expansion and phase transformations occurring in the surface region of the metal target. The dynamic boundary condition in this case takes the form of an imaginary plane that interacts with the Ag atoms through the Lennard-Jones (LJ) potential defined as a function of the distance between an Ag atom and the imaginary plane. The imaginary plane moves in response to forces acting on it from the Ag atoms as well as an additional force $\vec{F}_e$ that mimics the elastic response of the overlayer to forces acting from the side of the metal target. This additional force is proportional to the instantaneous velocity $\vec{v}$ of the imaginary plane and acts in the opposite direction, $\vec{F}_e = -Sz\vec{v}$, where S is the surface area of the interface and z is the acoustic impedance of the overlayer material. For the silica overlayer, the acoustic impedance is calculated as $z = \rho_{SiO_2} c_{SiO_2}$ where $\rho_{SiO_2} = 2.2\,\mathrm{g/cm^3}$ and $c_{SiO_2} = 5900$ m/s are the experimental values of density and speed of sound in fused silica.[36] The mass assigned to the imaginary plane is equal to the total mass of Ag atoms in a single (001) atomic plane and the equation of motion is solved for the plane together with the integration of the equations of motion for all the atoms.

The parameters of the LJ potential describing the interaction between a Ag atom and the imaginary plane are fitted to reproduce the experimental value of the work of adhesion between the Ag substrate and silica overlayer as well as the local stiffness under uniaxial compression at the interface defined by an arithmetic average of the elastic constant C_{11} for FBD EAM Ag ($C_{11} = 124$ GPa, Ref. 33) and fused silica ($C_{11} = 76.6$ GPa, calculated from experimental values of longitudinal wave velocity and density, Ref. 36). The work of

adhesion for Ag-silica interface at 773 K, $W_{adh} = 0.43\,J/m^2$ (Ref. 47) is used to fit the value of the LJ parameter defining the energy scale of the potential, ε. This parameter is chosen so that the energy of the Ag-silica interface, γ_{Ag-SiO_2}, satisfies the following definition of the work of adhesion: $W_{adh} = \gamma_{Ag} + \gamma_{SiO_2} - \gamma_{Ag-SiO_2}$, where $\gamma_{Ag} = 0.72\,J/m^2$ is the energy of free (001) surface of Ag calculated at 773 K for the FBD EAM potential and $\gamma_{SiO_2} = 0$ since the energy of the imaginary surface of silica after separation from Ag is zero. The small difference of the value of γ_{Ag} from the one reported in Ref. 33, $\gamma_{Ag} = 0.705\,J/m^2$, can be attributed to different temperature and the cutoff function applied in the current work. The parameter defining the length scale of the potential, σ, is then chosen to reproduce the local stiffness to uniaxial compression, C_{11}, as described above. The fitting yields the following parameters of the LJ potential: $\sigma = 2.42$ Å and $\varepsilon = 0.224$ eV.

While the representation of the overlayer by the method based on the imaginary plane provides a computationally efficient description of the partial reflection of the laser-induced pressure wave from the metal-silica interface and reproduces the experimental work of adhesion between the metal substrate and silica overlayer, this method is not free of limitations. In particular, the boundary condition can only reproduce the elastic response of the overlayer and no plastic deformation or melting of the overlayer is allowed. Moreover, in the simulations performed under irradiation conditions leading to the transient surface melting and resolidification of the metal target, the imaginary plane is observed to promote nucleation of hcp and fcc crystallites with close-packed crystallographic planes oriented parallel to the imaginary plane.

In order to relax the assumption of an ideal "indestructible" overlayer, an alternative method, illustrated in Fig. 1(b), is developed. In this method, a part of the overlayer adjacent to the metal target is simulated with an atomistic MD method. In the present work, we do not attempt to provide an accurate description of the silica structure and silica-Ag interfacial structure, as such description would necessitate the use of a reactive force field that would substantially increase the computational cost of the simulations. Instead, the silica substrate is simulated as an fcc crystal with atoms interacting through LJ potential. The parameters of the LJ potential ($\sigma = 4.41$ Å and $\varepsilon = 0.237$ eV) and the atomic mass of 113.5 Da are chosen so that the values of the elastic constant, $C_{11} = 75$ GPa, melting temperature, $T_m = 1825$ K, and density, $\rho_{SiO_2} = 2.2\,g/cm^3$ of the model material are in a good agreement with experimental values for fused silica ($C_{11} = 76.6$ GPa, $T_m = 1938$ K, $\rho_{SiO_2} = 2.2\,g/cm^3$, Ref. 36).

The cross-interaction between the atoms in the overlayer and Ag is also described by the LJ potential. The LJ parameter σ is chosen so that the equilibrium interatomic distance for the cross-interaction would be an arithmetic average of the ones in the substrate and the overlayer. Similarly to the case where the overlayer is represented by an imaginary plane (described above), the LJ parameter ε is fitted to the work of adhesion for the Ag-silica interface at 773 K, $W_{adh} = 0.43\,J/m^2$, Ref. 47. With the calculated surface energies of $\gamma_{Ag} = 0.72\,J/m^2$ and $\gamma_{SiO_2} = 0.39\,J/m^2$, the parameter ε is chosen to reproduce the energy of the Ag-silica interface, $\gamma_{Ag-SiO_2} = \gamma_{Ag} + \gamma_{SiO_2} - W_{adh} = 0.68\,J/m^2$. The fitting yields the following parameters of the LJ potential for the Ag-silica cross-interaction: $\sigma = 3.53$ Å, $\varepsilon = 0.111$ eV.

The size of the part of the overlayer represented with atomistic resolution, L_{MD} in Fig. 1(b), is 100 nm in simulations performed at absorbed laser fluences of 900 and $1000\,J/m^2$, and 200 nm at 3000 and $6000\,J/m^2$. In contrast to the metal substrate, where the heat transfer is dominated by the electrons and is reproduced with the TTM equations, the vibrational heat transfer in the glass overlayer is treated directly by the MD model. The value of the thermal conductivity of the model overlayer material, $k \approx 0.85\,Wm^{-1}K^{-1}$, is calculated from the evolution of the temperature profiles predicted in a non-equilibrium MD simulation of a 411 nm long system with an initial temperature of 300 K and a temperature of 1000 K fixed at one end of the system. The conductivity of the model material is comparable to the experimental one for fused silica, $1.38\,Wm^{-1}K^{-1}$, Ref. 36. The characteristic length of thermal diffusion in the simulated overlayer on the timescale of the simulation, $t_{sim} = 1$ ns, is $L_{th} = \sqrt{2D_T t_{sim}} \approx 57$ nm, where $D_T = k/c_v \sim 1.7 \times 10^{-6} m^2/s$ is the thermal diffusivity, k is the thermal conductivity, $c_v \approx 3R$ is the heat capacity, and R is the ideal gas constant. Therefore, for $L_{MD} = 100 - 200$ nm, $L_{th} < L_{MD}$ and the heat transfer through the upper boundary of the computational system in Fig. 1(b) is neglected in the simulations. A pressure-transmitting boundary condition,[45,46] similar to the one applied at the bottom of the TTM-MD region of the metal target, is applied to the top monolayer of the fcc crystal representing the MD part of the overlayer. The parameters of the boundary condition are chosen to minimize the reflection of the pressure wave propagating through the overlayer from the metal-overlayer interface. Before applying the laser irradiation, all systems are equilibrated at 300 K for 200 ps.

III. RESULTS AND DISCUSSION

To reveal the effect of the transparent overlayer on laser-induced processes, two series of simulations, with and without the overlayer, are performed for a range of laser fluences that covers the regimes of surface melting, photomechanical spallation, and phase explosion in the absence of the overlayer. The presentation of the results of the simulations is preceded by a brief discussion of the concepts of thermal, stress, and spatial confinement.

A. Thermal, stress, and spatial confinement in laser-materials interactions

Before discussing the effect of the *spatial confinement* on the material response to the laser excitation, we would like to distinguish it from the *thermal* and *stress confinement* realized when the characteristic times of the redistribution of the absorbed laser energy by thermal conduction or stress waves are longer than the time of the temperature increase due to the laser energy deposition.[21,22,27,37,48,49] The condition for the thermal confinement, in particular, can be expressed as $\max\{\tau_p, \tau_{e-ph}\} \leq L_c^2/(2D_T)$, where τ_p is the

laser pulse duration, τ_{e-ph} is the characteristic time of the electron-phonon equilibration, L_c is the diffusive/ballistic penetration depth of the excited electrons before the electron-electron and the electron-phonon equilibration, and D_T is the thermal diffusivity of the target material. The condition for the stress confinement can be expressed as $\max\{\tau_p, \tau_{e-ph}\} \leq L_c/C_s$, where C_s is the speed of sound in the target material.

In the simulations of Ag targets irradiated by 10 ps laser pulses, $\tau_p = 10$ ps, $\tau_{e-ph} \approx 8$ ps (defined as the timescale of the exponential decay of the energy of the excited electrons due to the electron-phonon coupling), $L_c \approx 140$ nm (defined as the depth where 63% of the total excitation energy is deposited by the time τ_{e-ph}), $D_T = 1.47 \times 10^{-4}$ m^2/s (in the solid state near the melting temperature), and $C_s = 3650$ m/s, Ref. 36), the conditions for both thermal and stress confinement are satisfied and a build up of both thermal energy and the thermoelastic compressive stresses can be expected in the regions of the laser energy thermalization during the laser pulse.[21,22,26–29] The conditions of the thermal and stress confinement have similar effect on targets with and without the transparent overlayer, thus suggesting that the initial levels of temperature and pressure generated in both cases are likely to be similar.

In contrast to the thermal and stress confinement that define the initial temperature raise and pressure build up in the surface region of the irradiated target, the spatial confinement by the transparent overlayer is affecting the longer-term material response to the laser energy deposition and can have a significant effect on the laser-induced phase transformations, generation of crystal defects, surface damage, and material removal (ablation). The results of the atomistic simulations reported below are providing first detailed insights into the kinetics and mechanisms of the structural and phase transformations occurring under conditions of spatial confinement by a transparent overlayer.

B. Melting and resolidification under spatial confinement

The effect of the spatial confinement on the processes of melting and resolidification induced by the laser energy deposition is illustrated in Fig. 2, where the temperature and pressure evolution is shown for three simulations performed at the same absorbed laser fluence of 900 J/m^2. For a bulk Ag target with a free surface, in the absence of the overlayer, this fluence is about 10% above the threshold for surface melting. The energy transfer from the excited electrons to the lattice leads to a rapid temperature increase in a surface region of the target, Fig. 2(a). The temperature exceeds the equilibrium meting temperature of the EAM Ag, $T_m = 1139$ K at zero pressure, causing a rapid homogeneous melting of ~35 nm thick surface layer between 40 and 70 ps of the simulation time (15 and 45 ps after the time of the laser peak intensity). The steep temperature gradient established in the surface region by the end of the electron-phonon equilibration leads to the cooling of the melted region and causes epitaxial resolidification. The velocity of the solidification front increases with increasing degree of undercooling below the melting temperature and the front reaches the surface of the target by the time of ~1.1 ns.

In the simulations performed for targets covered by an overlayer, Figs. 2(b) and 2(c), the melting is limited to a few small regions transiently appearing in the vicinity of the interface with the overlayer and disappearing by the time of 400 ps. In the simulation where the overlayer is represented by an imaginary plane, Fig. 2(b), the melting affects a thin (<4 nm) layer adjacent to the interface with the overlayer and another region that appears through homogeneous nucleation at a depth of about 10 nm below the interface. A very similar transient melting is observed in the simulation with the atomistic representation of the overlayer, Fig. 2(c), where two small melting regions transiently appear within 20 nm from the interface with the overlayer. The difference of these results from the much more extensive melting observed in the absence of the overlayer, Fig. 2(a), is surprising from the first sight, as the same initial temperature increase is caused by the laser energy deposition and the temperature decrease is even faster in the case of free surface due to the rapid expansion of the surface region. To explain this difference, the evolution of the laser-induced pressure is considered below.

As discussed in Sec. III A, the rapid increase of the lattice temperature in the simulations takes place under conditions of the stress confinement and results in the buildup of strong compressive stresses in the surface region of the irradiated target. The generation of compressive stresses of similar strength can be seen in all pressure plots shown in Fig. 2. The relaxation of the compressive stresses, however, proceeds differently with and without the confining overlayer. Without the overlayer, the expansion of the compressed material results in the generation of a strong tensile component of the stress wave that follows the compressive component in its propagation into the bulk of the target, Fig. 2(a). In the presence of the overlayer, however, the tensile component of the stress wave is largely suppressed, Figs. 2(b) and 2(c). Since the acoustic impedance of the overlayer material is more than twice smaller than one of Ag, the relaxation of the initial laser-induced compressive stresses results the generation of both a compressive wave in the overlayer and a relatively weak unloading wave in the Ag target.

The suppression of the tensile component of the pressure wave by the overlayer has direct implications for the melting process. In the absence of the overlayer, the expansion of the surface region results in the tensile stresses and, concurrently, a transient temperature drop that can be estimated by considering the expansion as an isentropic process for which $(\partial T/\partial P)_S = T\alpha/c_p$,[18,32] where c_p is the specific heat capacity per unit volume and α is the volume coefficient of thermal expansion. At the same time, the equilibrium melting temperature is also affected by the negative stresses, with the variation of the melting temperature described by the Clapeyron equation, $(dT/dP)_m \approx \Delta V_m/\Delta S_m$, where ΔV_m and ΔS_m are the volume change upon melting and the entropy of melting, respectively. Following an approach described in Ref. 32, the thermodynamic parameters of the FBD EAM Ag, $\Delta V_m = 0.81$ cm^3/mol, $\Delta H_m = 12\,350$ J/mol, $\Delta S_m = \Delta H_m/T_m = 10.84$ J/(mol K), as well as $\alpha = 102 \times 10^{-6}$ K^{-1} and $c_p = 31.8$ J/(mol K) $= 2.85$ J/(cm^3 K) for the solid phase

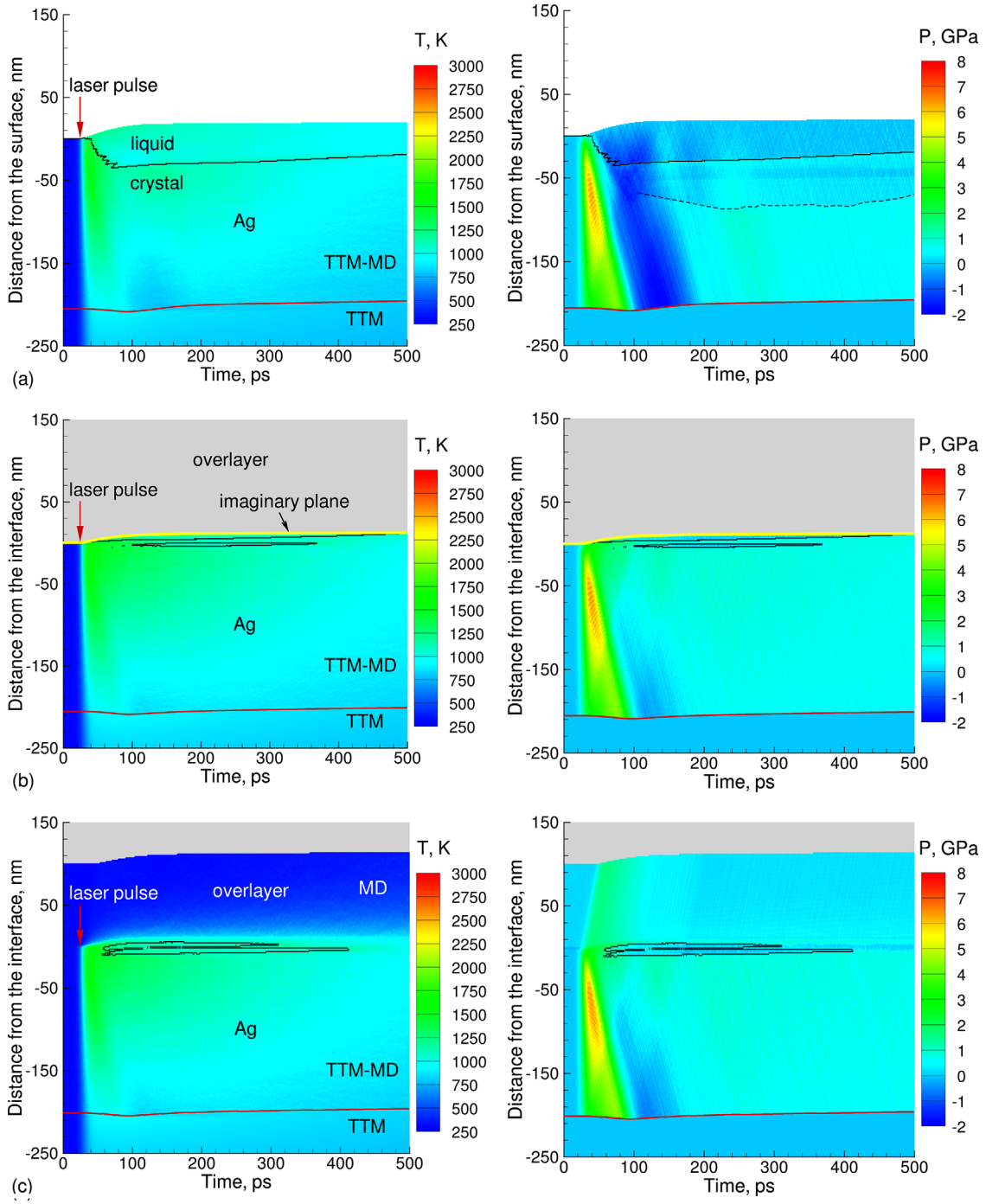

FIG. 2. Temperature (left) and pressure (right) contour plots in simulations of a bulk Ag target irradiated by a 10 ps laser pulse at a fluence of 900 J/m^2. The irradiated surface is free of confinement in (a) and is covered by a transparent overlayer in (b) and (c). The overlayer is represented by a dynamic imaginary plane in (b) and by an atomistic MD description of a part of the overlayer adjacent to the Ag target combined with a pressure-transmitting boundary condition in (b). The laser pulse has a Gaussian profile with the peak intensity reached at 25 ps from the beginning of the simulations and is directed along the Y-axis, as shown by the red arrows in the left panels. The black curves separate the melted regions from crystalline parts of the Ag target. The red curves separate the atomistic (TTM-MD) and continuum (TTM) parts of the model representing the Ag targets. The dashed curve in the pressure plot in (a) shows the maximum depth of dislocation propagation. The yellow curves in (b) show the position of the Ag-overlayer interface represented by the dynamic imaginary plane.

at $T \approx T_m$ and zero pressure have been evaluated based on the temperature dependences of volume and internal energy of liquid and solid phases at constant pressure. With these thermodynamic parameters, $(dT/dP)_m \approx 74$ K/GPa and $(\partial T/\partial P)_S \approx 41$ K/GPa for the solid phase close to the melting temperature and zero pressure. The steeper slope of the liquid-crystal coexistence line compared to the isentrope for the solid phase, $(dT/dP)_m > (\partial T/\partial P)_S$, typical for metals, suggests that the expansion of the target by the unloading wave facilitates melting despite simultaneously causing a transient cooling of the material. This explains why the partial suppression of the generation of the unloading wave also suppresses melting in the simulations of Ag targets covered by overlayers.

An examination of the pressure contour plots in Fig. 2 also reveals that, in all simulations, the propagation of the

unloading wave takes place on a background of quasi-static compressive stresses related to the inability of the crystalline part of the target to completely relax the thermoelastic stresses through uniaxial expansion in the direction normal to the irradiated surface or metal-overlayer interface.[21,26,27] The compressive stresses are partially relaxed by the emission of dislocations from the melting front in the simulation with free surface, Fig. 2(a), where the depth of the dislocation propagation can be seen from the reduction of the compressive stresses in a region extending down to ~45 nm below the melting front. The emission of the dislocations coincides with the propagation of the unloading wave through the melting front and is triggered by the shear stresses transiently created by the unloading wave in the four different active {111} slip planes of the single crystal fcc target oriented along ⟨100⟩ direction.[50] Interactions between the Shockley partial dislocations propagating on different slip planes result in the generation of immobile dislocation segments and formation of stable dislocation configurations in the sub-surface region of the target. The much weaker unloading wave generated in the presence of the overlayer is incapable of inducing the dislocation emission and no dislocations are observed in simulations illustrated in Figs. 2(b) and 2(c).

The results obtained with two different representations of the overlayer, Figs. 2(b) and 2(c), are very similar to each other. This similarity suggests that both approaches provide an adequate description of the effect of the overlayer on the target response to the laser excitation under irradiation conditions that leave the overlayer intact. At higher laser fluences, however, a part of the overlayer adjacent to the metal target can be expected to undergo transient melting and possible mixing with the melted metal. To provide a semi-quantitative description of these processes, the atomistic representation of a part of the overlayer adjacent to the metal target (Fig. 1(b)) is used in the higher-fluence simulations presented below.

C. Suppression of laser spallation by the overlayer

A moderate increase in the absorbed laser fluence from 900 J/m^2 to 1000 J/m^2 leads, in the absence of overlayer, to the transition from the regime of melting and resolidification of a surface region of the target to a separation of a melted layer from the bulk of the target, Fig. 3(a). As discussed in a number of earlier papers, e.g., Refs. 21, 22, and 27–29, the separation and ejection of the liquid layer (commonly

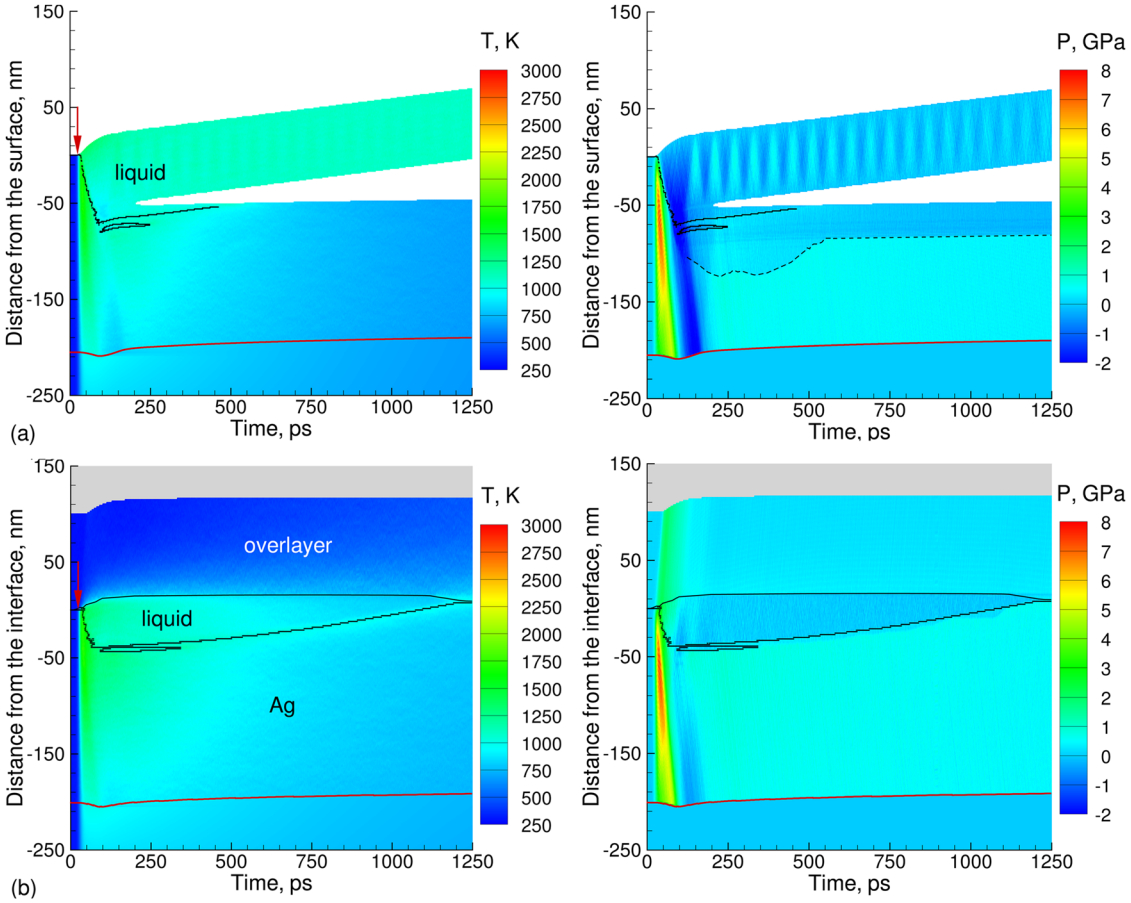

FIG. 3. Temperature (left) and pressure (right) contour plots in simulations of a bulk Ag target irradiated by a 10 ps laser pulse at a fluence of 1000 J/m^2. The irradiated surface is free of confinement in (a) and is covered by a transparent overlayer in (b). The computational setup in the simulation with overlayer is illustrated in Fig. 1(b). The laser pulse has a Gaussian profile with the peak intensity reached at 25 ps from the beginning of the simulations and is directed along the Y-axis, as shown by the red arrows in the left panels. The black curves separate the melted regions from crystalline parts of the Ag target. The red curves separate the atomistic (TTM-MD) and continuum (TTM) parts of the model representing the Ag targets. The dashed curve in the pressure plot in (a) shows the maximum depth of dislocation propagation. Areas where the density of the material drops below 10% of the initial density of the solid Ag target are blanked in the plots.

referred to as spallation) is driven by the relaxation of the laser-induced stresses generated in the surface region of the target under conditions of stress confinement. The magnitude of both the compressive and tensile stresses increases with increasing fluence up to the spallation threshold, when the tensile stress exceeds the dynamic strength of the melted material leading to the nucleation, growth, and coalescence of multiple voids that eventually causes spallation of a liquid layer from the target. The spallation interrupts the heat flow from the hot surface layer to the bulk of the target and results in a rapid resolidification of the liquid part of the target left behind after the separation of the spalled layer. In the simulation illustrated in Fig. 3(a), the resolidification process is completed at ~550 ps after the laser pulse. Similarly to the lower fluence simulation discussed in Sec. III B, the emission of dislocations from the melting front takes place at the time when the tensile component of the stress wave crosses the melting front. The plastic deformation partially relaxes the residual compressive stresses in ~40 nm surface region of the resolidified target.

Turning to the simulation of a Ag target covered by an overlayer, Fig. 3(b), the following effects of the spatial confinement can be observed: (1) the depth of the region affected by melting decreases from ~70 nm in Fig. 3(a) to ~40 nm in Fig. 3(b), (2) no dislocation emission from the melting front takes place, and (3) no voids nucleate in the melted region and no spallation occurs. All of these effects can be attributed to the containment of the free expansion of the surface region of the target and the corresponding suppression of the tensile component of the stress wave.

The suppression of the tensile stresses is illustrated in Fig. 4, where the evolution of pressure at a depth of 100 nm below the irradiated Ag surface is shown in the form of pressure profiles. Although the initial peaks of the compressive pressure are almost identical in the two simulations, with the maximum pressure reaching ~6.7 GPa at ~45 ps after the laser pulse, the pressure profiles diverge after ~70 ps. In the case of free surface, the unloading tensile component of the pressure wave, while weakened by the void nucleation and spallation in the region closer to the surface, is still clearly pronounced and reaches the maximum value of −2 GPa. In the presence of the overlayer, however, the pressure at this depth remains positive at all times. Following the initial dynamic relaxation of the laser-induced stresses, after ~250 ps, the level of pressure stays at an almost constant level that is slowly drifting from ~0.8 to 0.6 GPa during the time from 250 to 700 ps. As discussed in Sec. III B, this compressive pressure corresponds to the residual thermoelastic stresses that cannot relax by the uniaxial expansion of the crystal in the direction normal to the surface and are slowly decreasing due to the cooling by thermal conduction to the bulk of the target.

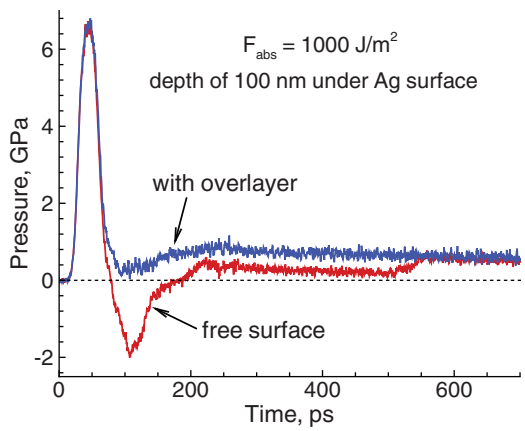

FIG. 4. Pressure profiles at a depth of 100 nm below the initial surface of Ag targets in simulations performed with and without the transparent overlayer and illustrated by contour plots in Fig. 3.

Note that the level of the residual stresses in the simulation with free surface stays at a lower level of ~0.2 – 0.3 GPa until the time of ~530 ps, when it increases to the level similar to the one observed in the presence of the overlayer. The reduction of the compressive stresses can be attributed to dislocations that propagate deeper than 100 nm during the initial relaxation of laser-induced stresses and bring the stress state of the crystal closer to hydrostatic one. The partial dislocations retreat up to the depth of ~80 nm below the original surface during the time of 400–600 ps and the increase of the level of pressure at around 530 ps corresponds to the time when they cross the depth of 100 nm.

In the absence of spallation, the resolidification process in the target covered by an overlayer takes about 1.25 ns, Fig. 3(b), the time comparable to that in the simulation of a target with free surface performed at a lower fluence of 900 J/m^2, below the spallation threshold, Fig. 2(a). The melting turns into resolidification when the temperature of the liquid-solid interface drops below the melting temperature at ~150 ps, the solidification front accelerates with increasing supercooling and reaches its maximum velocity of ~65 m/s by the time of 1.1 ns. By this time, however, the temperature of Ag near the interface with the overlayer drops down to ~0.7 T_m, triggering nucleation of new crystallites near the interface and leading to the rapid solidification of the strongly supercooled layer of Ag adjacent to the interface. The relatively small lateral size of the computational cell used in the simulations does not allow for a reliable investigation of the nucleation and growth of new crystallites in the supercooled interfacial region of the target and additional larger scale simulations targeted at analysis of this phenomenon are currently underway.

D. Suppression of phase explosion by the overlayer

As the laser fluence increases above the spallation threshold for targets with free surfaces, the thickness of the spalled layer is decreasing while the temperature and the ejection velocity are increasing.[29] The spalled layer vanishes close to the fluence that brings the temperature of the surface region of the target above $T^* = 3450$ K, identified in Sec. II A as the temperature of the onset of the explosive phase separation into liquid and vapor at zero pressure. This signifies a transition to the phase explosion regime of material ejection, when the surface region of the target undergoes an explosive decomposition into vapor, clusters, and small droplets.

The contour plots shown in Fig. 5(a) are for a simulation performed at a fluence of 3000 J/m^2, slightly above the

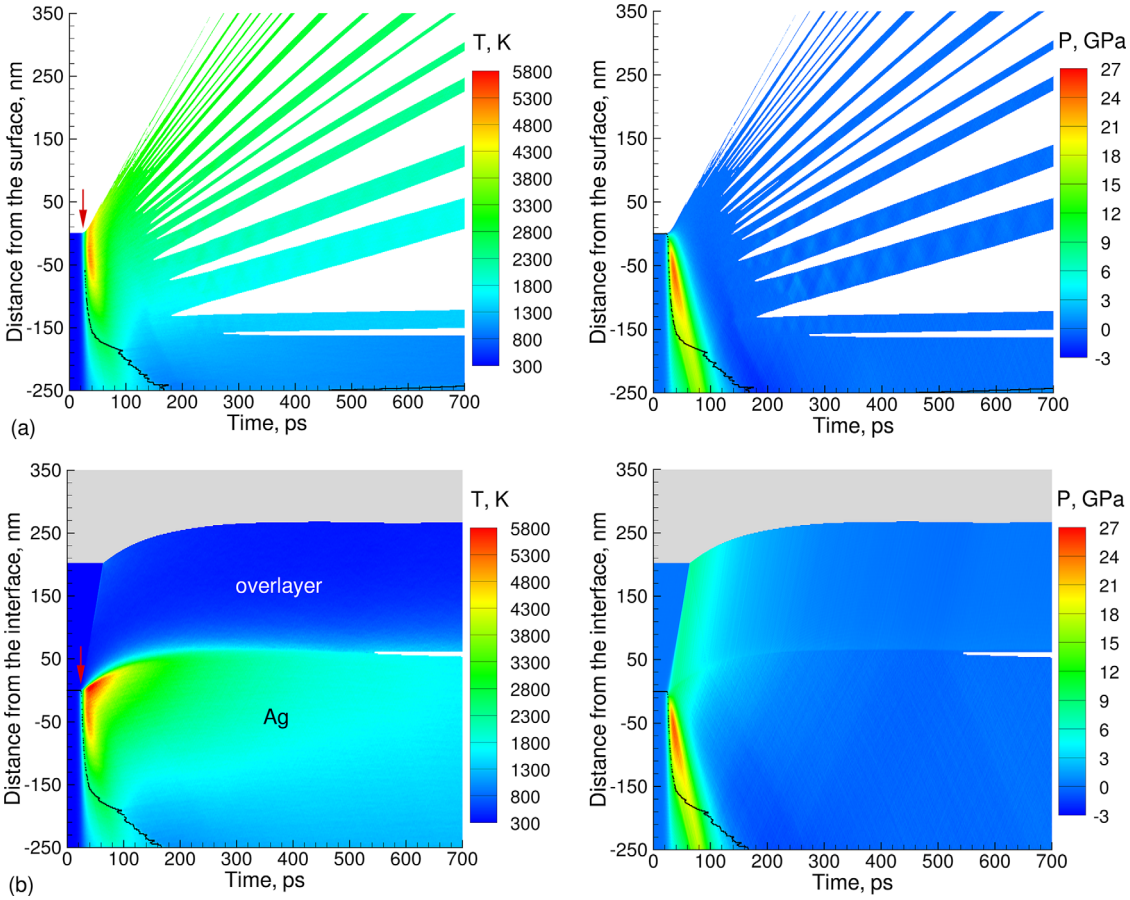

FIG. 5. Temperature (left) and pressure (right) contour plots in simulations of a bulk Ag target irradiated by a 10 ps laser pulse at a fluence of 3000 J/m^2. The irradiated surface is free of confinement in (a) and is covered by a transparent overlayer in (b). The computational setup in the simulation with overlayer is illustrated in Fig. 1(b). The laser pulse has a Gaussian profile with the peak intensity reached at 25 ps from the beginning of the simulations and is directed along the Y-axis, as shown by the red arrows in the left panels. The black curves separate the melted regions from crystalline parts of the Ag target. Areas where the density of the material drops below 10% of the initial density of the solid Ag target are blanked in the plots.

threshold for the transition from spallation to the phase explosion regimes of laser ablation. The temperature plot exhibits a momentary (between 30 to 60 ps of the simulation, or 5 to 35 ps after the peak intensity of the 10 ps laser pulse) spike to the values exceeding T^* at zero pressure in the surface region with a depth of ~115 nm, close to the depth of the initial laser energy deposition L_c, see Sec. III A. The rapid cooling of this region proceeds through the expansion and decomposition of the material overheated above the limit of its thermodynamic stability into a mixture of liquid droplets, atomic clusters, and vapor. The unloading wave, while partially suppressed by the compressive pressure generated by the explosive decomposition and expansion of the top layer of the target, still generates tensile stresses that exceed −1 GPa below the depth of ~140 nm. These tensile stresses induce cavitation of the superheated liquid deeper into the target and, similarly to the spallation discussed above, lead to the ejection of additional large droplets.

In contrast to the explosive decomposition of a surface region discussed above, no phase separation is observed in a simulation performed at the same laser fluence for a target covered by an overlayer, Fig. 5(b). The initial temperature increase is similar to the one in a target with free surface and brings the surface region to a supercritical state. Although the pressure from the hot metal pushes the overlayer up by 65 nm, the supercritical fluid remains confined by the overlayer. This confinement prevents the phase decomposition and fast cooling observed for a target with free surface and keeps the temperature and pressure of the surface region at high levels for a much longer time. Only by the time of 350 ps, the pressure in the interfacial region drops down to zero and the expansion of the metal target turns into contraction as the interfacial region continues to cool down by thermal conduction to the bulk of the target. The contraction results in the formation of voids near the interface and eventual detachment of the metal target from the overlayer. In the absence of the phase explosion, which provides an efficient channel of fast cooling of the hot surface region of the target with free surface, the maximum melting depth is larger (270 nm vs 250 nm in the simulation with free surface) and the time needed for resolidification of the metal target is much longer. The emission of partial dislocations, though, is observed at this fluence both with and without overlayer.

An additional illustration of the effect of spatial confinement by the overlayer on the conditions experienced by the top layer of the metal target is provided in Fig. 6, where the temperature-pressure trajectories are shown for material initially located within the top 5 nm layer of the target. In the simulation with free surface, the initial linear pressure-temperature dependence characteristic of almost constant

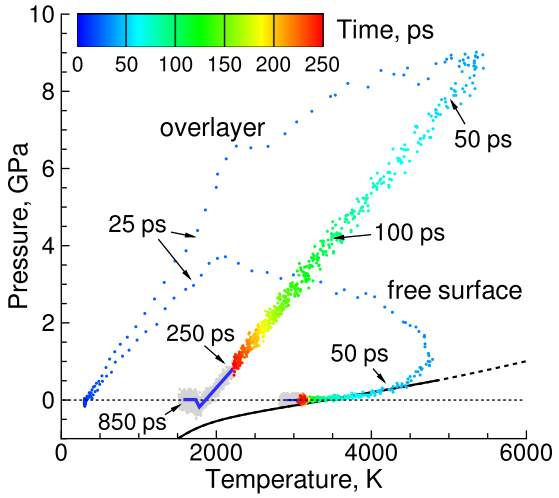

FIG. 6. The evolution of temperature and pressure averaged over atoms that are initially located in the top 5 nm thick layer of the Ag target irradiated by 10 ps laser pulses at a fluence of 3000 J/m^2 with and without the presence of a transparent overlayer. The points along the trajectories are colored by time up to 250 ps as shown by the legend; from 250 to 850 ps, the points are gray with blue lines drawn as a guide to the eye. The black curve shows the temperature–pressure conditions (T*, P*) for the onset of the cavitation or phase explosion in the metastable liquid, calculated for the EAM Ag material as explained in Sec. II A.

volume heating of the layer (stress confinement) gives way to the pressure drop associated with the onset of free expansion of the top layer at ~25 ps. The relaxation of the laser-induced pressure and continued temperature increase makes the trajectory cross the solid curve that marks the temperature and pressure conditions for the onset of the explosive phase separation into liquid and vapor, T^* and P^*, determined as explained in Sec. II A. In the presence of overlayer, however, the expansion of the hot metal layer is limited and the pressure builds up to much higher levels. The expansion of the surface allowed by up to 65 nm upward displacement of the overlayer results in a pressure plateau at the end of the electron-phonon energy equilibration and leads to a hysteresis in the pressure-temperature dependence, when the pressure decreases during the cooling of the interfacial region along the path that is almost parallel to the one of the heating stage but shifted to lower values of pressure for the same temperature. This hysteresis eventually leads to the detachment of the metal target from the overlayer when the pressure near the interface becomes negative after about 400 ps, when the temperature drops below 1800 K.

The overall picture of the material response to the laser energy deposition with and without the overlayer does not change even when the laser fluence is doubled from 3000 J/m^2 to 6000 J/m^2, Figs. 7 and 8. The much stronger laser excitation leads to higher maximum temperature and pressure, larger displacement of the overlayer, and higher melting depths of 455 and 415 nm with and without overlayer, respectively. The combination of the phase explosion and material expulsion due to the unloading wave leads to almost complete ejection of melted part of the target down to the depth of 385 nm in the case of the target with a free surface, Fig. 7(a). In the presence of the overlayer, the expansion of the metal brought to the supercritical state by the fast laser energy deposition is limited by the overlayer that maintains the high density and pressure of the supercritical fluid for hundreds of ps and prevents its decomposition into vapor and liquid droplets. The pressure exerted by the supercritical Ag pushes the overlayer by up to 137 nm by the time of 600 ps, when the pressure approaches zero level, Fig. 7(b). Similarly to the lower fluence simulation illustrated in Fig. 5(b), the cooling and contraction of the metal target lead to its detachment from the overlayer at around 800 ps, Fig. 7(b). The temperature of the metal near the interface is about 2500 K, more than twice above the melting temperature but below the stability limit for phase explosion. Due to the high temperature of the interfacial region, the detachment takes place at a relatively low negative pressure of about −0.11 GPa (this value is obtained by averaging from 700 to 800 ps over the top 50 nm part of the metal target).

The temperature-pressure trajectories shown in Fig. 8 further illustrate the difference in thermodynamic conditions experienced by the material in the top surface layers of the two targets. While in both simulations, the strong laser excitation brings the layers into supercritical state, the evolution of the supercritical fluid is very different in the two cases. In the absence of overlayer, free expansion of the supercritical fluid releases the pressure and results in complete vaporization of the material. The supercritical fluid confined by the overlayer, on the other hand, slowly cools down from the supercritical to the liquid state without crossing the line that corresponds to the explosive phase separation.

The observation that the maximum temperature of the top region reaches ~12 000 K in the simulation with overlayer and ~11 000 K without overlayer by the time of ~40 ps suggests the possibility of ionization of a fraction of Ag atoms. Indeed, estimations based on the Saha equation yields ionization fraction of about 1% at densities realized during the peak temperatures. The short time of the temperature spike (the temperature drops down to 9000 K by 80 ps and down to 6000 K by 170 ps in the simulation with overlayer, where the cooling is slower) and the high density of the supercritical fluid indicate, however, that any effects related to the ionization and charge fluctuations[40] in the supercritical fluid are likely to have negligible effect on the material expansion and interaction with the overlayer under conditions considered in the simulations.

The exposure of the overlayer to the hot metal leads to the melting of a part of the overlayer adjacent to the metal target, with the thickness of the melted layer reaching 15 nm by the time of the detachment from the target. The interaction of the supercritical Ag with melted overlayer results in an active atomic mixing in the interfacial region. The mixing is illustrated in Fig. 9, where the atomic configurations and concentration profiles in the vicinity of the metal-overlayer interface are shown for 780 ps, just before the detachment of the metal from the overlayer. The observation that more atoms of the overlayer material penetrate into the metal can be explained by much higher temperatures of the metal and a relatively weak interaction between the overlayer and Ag atoms. The Ag atoms are also diffusing into the melted part of the overlayer and tend to aggregate into clusters due to the stronger interactions between the metal atoms as compared

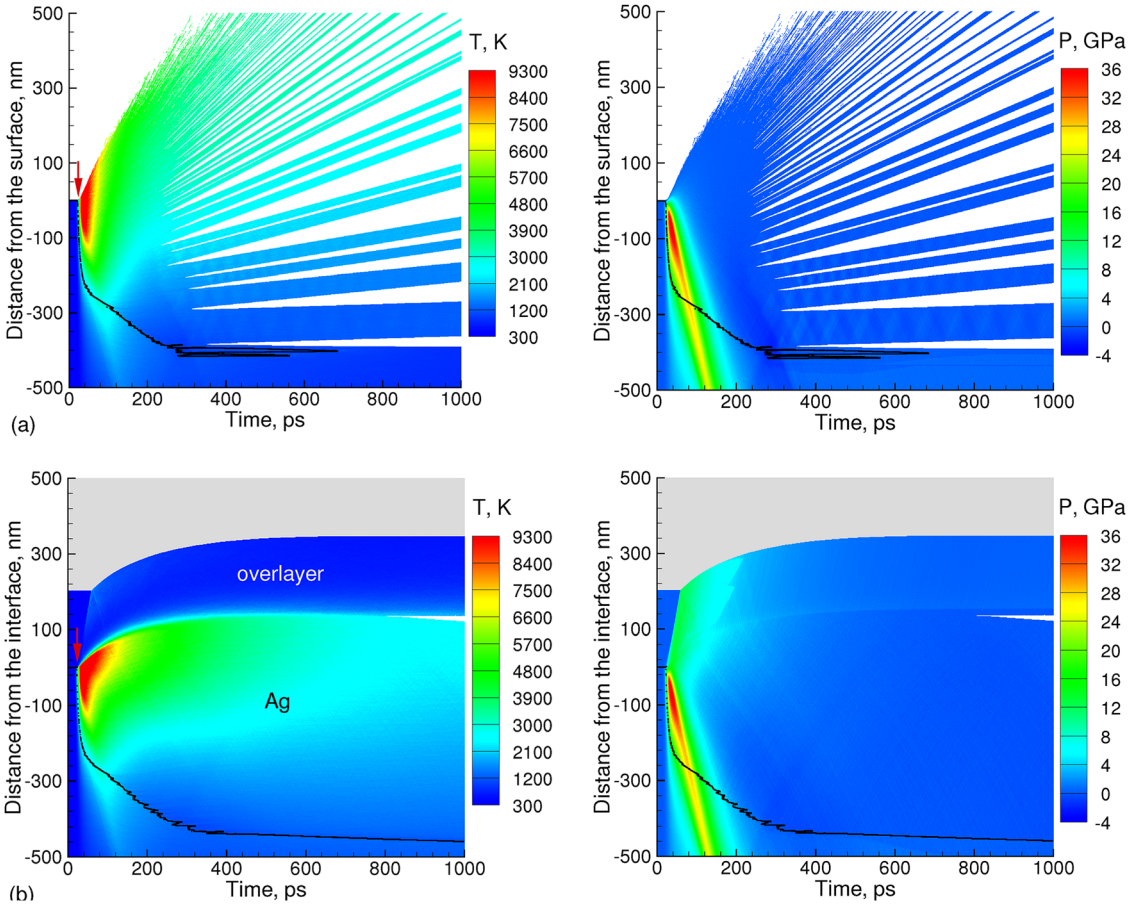

FIG. 7. Temperature (left) and pressure (right) contour plots in simulations of a bulk Ag target irradiated by a 10 ps laser pulse at a fluence of 6000 J/m^2. The irradiated surface is free of confinement in (a) and is covered by a transparent overlayer in (b). The computational setup in the simulation with overlayer is illustrated in Fig. 1(b). The laser pulse has a Gaussian profile with the peak intensity reached at 25 ps from the beginning of the simulations and is directed along the Y-axis, as shown by the red arrows in the left panels. The black curves separate the melted regions from crystalline parts of the Ag target. Areas where the density of the material drops below 10% of the initial density of the solid Ag target are blanked in the plots.

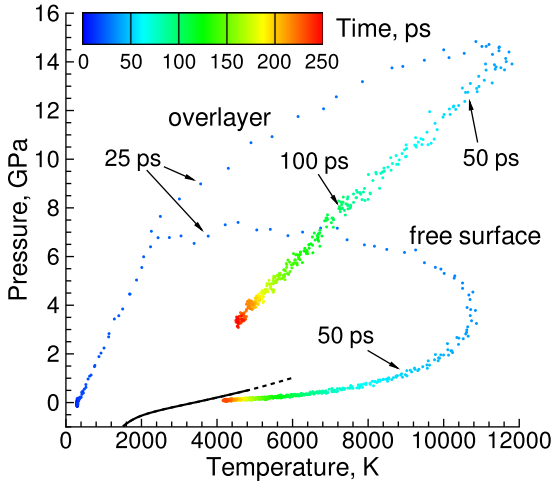

FIG. 8. The evolution of temperature and pressure averaged over atoms that are initially located in the top 5 nm thick layer of the Ag target irradiated by 10 ps laser pulses at a fluence of 6000 J/m^2 with and without the presence of a transparent overlayer. The points along the trajectories are colored by time as shown by the legend. The black curve shows the temperature–pressure conditions (T*, P*) for the onset of the cavitation or phase explosion in the metastable liquid, calculated for the EAM Ag material as explained in Sec. II A.

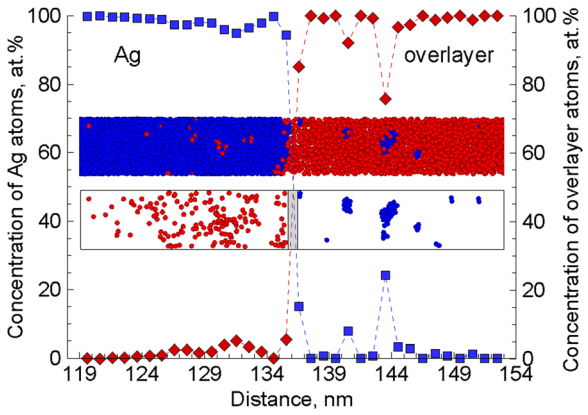

FIG. 9. Concentration profiles and atomic configuration in the region of Ag-overlayer interface at 780 ps after irradiation by a 10 ps laser pulse at a fluence of 6000 J/m^2. The atoms in the snapshot are colored by their type, with blue and red colors used for Ag and overlayer atoms, respectively. In the lower version of the snapshot, the Ag atoms are blanked on the left side of the interface and the overlayer atoms are blanked on the right side of the interface to expose the atomic mixing.

to the metal-overlayer interactions. Note that the approximate representation of the overlayer by atoms interacting with each other through pairwise LJ potential prevents a quantitative analysis of the atomic mixing and formation of new phases in the interfacial region. At a qualitative level, however, we can conclude that a substantial interfacial mixing can be expected to result in a high concentration of impurities, atomic clusters, and/or new phases on both the overlayer and metal sides of the interface. A quantitative analysis of the nanostructure of the interfacial region can be performed by adopting the computational setup shown in Fig. 1(b) for simulations with a realistic representation of interatomic interactions accounting for the mixed covalent-metallic nature of bonding in the interfacial region.

IV. SUMMARY

The effect of spatial confinement on laser-induced structural and phase transformation in a metal target is investigated by contrasting the results of two series of simulations of short pulse laser interactions with a bulk Ag target. The metal target is covered by a thick transparent overlayer in one series of simulations and has a free surface in the other series. The simulations are performed with a combined atomistic-continuum TTM-MD model accounting for the laser excitation of conduction band electrons, electron-phonon equilibration, as well as electronic and phononic heat transfer in the metal target and the overlayer. The model is extended by incorporation of two alternative computational methods for representations of the transparent overlayer. In one method, the layer is represented by a dynamic acoustic impedance matching boundary condition designed to represent the partial propagation of the laser-induced pressure wave into the overlayer, as well as the work of adhesion between the metal and the overlayer. In the second method, a part of the overlayer is represented with atomic resolution, allowing not only to account for the elastic response of the overlayer but also to reproduce the plastic deformation, melting, and atomic mixing in the region of the overlayer adjacent to the hot metal target. Both methods are parameterized for Ag-silica system and show similar performance at low fluences, when no melting of the overlayer takes place. The second (atomistic) representation of the metal-overlayer interface is used in the simulations performed at high fluences, when melting and atomic mixing take place on both sides of the interface.

The simulations are performed for a broad range of laser fluences that, in the absence of overlayer, covers the regimes of melting and resolidification, photomechanical spallation, and phase explosion of the surface region of the metal target. At low fluences that correspond to melting and spallation of targets with free surfaces, the spatial confinement by the overlayer is found to suppress the generation of the unloading tensile wave, decrease the maximum depth of melting, reduce or eliminate the emission of dislocations from the melting front, and prevent the cavitation and spallation in the surface region of the metal target.

At higher fluences that bring the surface region of the metal target to the supercritical state, the confinement prevents the expansion and explosive phase decomposition of the surface region and leads to a gradual cooling of the hot and compressed supercritical fluid down to the liquid phase. This is in a sharp contrast with the material response to the same laser energy deposition under the vacuum conditions (free surface of the target), when the free expansion of the supercritical fluid results in a rapid cooling and phase decomposition into liquid droplets and vapor or complete vaporization of the top surface layer at higher fluences. The confinement of the superheated metal by the overlayer increases the maximum depth of melting and the time required for resolidification after the laser pulse. Moreover, the relatively long lifetime of the supercritical state sustained under conditions of spatial confinement results in a transient melting of a part of the overlayer exposed to the hot metal and atomic mixing between the overlayer material and metal within tens of nanometers from the interface. The simulations also suggest the possibility of detachment of the metal target from the overlayer during the rapid cooling and contraction of the surface region of the metal target. A detailed analysis of the evolution of voids leading to the detachment at the interface as well as the possible formation of a thin multiphase nanocrystalline layer due to the atomic mixing and rapid resolidification of the target requires simulations with larger lateral size of the computational system and a more realistic description of interatomic interactions in the interfacial region.

ACKNOWLEDGMENTS

Financial support for this work was provided by Electro Scientific Industries, Inc., the National Science Foundation (NSF) through Grants DMR-0907247 and CMMI-1301298, and the Air Force Office of Scientific Research through Grant FA9550-10-1-0541. Computational support was provided by the Oak Ridge Leadership Computing Facility (Projects MAT048) and NSF through the Extreme Science and Engineering Discovery Environment (Project TG-DMR110090).

[1]B. P. Fairand, B. A. Wilcox, W. J. Gallagher, and D. N. Williams, "Laser shock-induced microstructural and mechanical property changes in 7075 aluminum," J. Appl. Phys. **43**, 3893–3895 (1972).
[2]R. Fabbro, J. Fournier, P. Ballard, D. Devaux, and J. Virmont, "Physical study of laser-produced plasma in confined geometry," J. Appl. Phys. **68**, 775–784 (1990).
[3]P. Peyre and R. Fabbro, "Laser shock processing: a review of the physics and applications," Opt. Quantum Electron. **27**, 1213–1229 (1995).
[4]X. Wu, Z. Duan, H. Song, Y. Wei, X. Wang, and C. Huang, "Shock pressure induced by glass-confined laser shock peening: Experiments, modeling and simulation," J. Appl. Phys. **110**, 053112 (2011).
[5]J. Bohandy, B. F. Kim, and F. J. Adrian, "Metal deposition from a supported metal film using an excimer laser," J. Appl. Phys. **60**, 1538–1539 (1986).
[6]I. Zergioti, S. Mailis, N. A. Vainos, C. Fotakis, S. Chen, and C. P. Grigoropoulos, "Microdeposition of metals by femtosecond excimer laser," Appl. Surf. Sci. **127–129**, 601–605 (1998).
[7]M. Domke, S. Rapp, M. Schmidt, and H. P. Huber, "Ultra-fast movies of thin-film laser ablation," Appl. Phys. A **109**, 409–420 (2012).
[8]G. Heise, M. Englmaier, C. Hellwig, T. Kuznicki, S. Sarrach, and H. P. Huber, "Laser ablation of thin molybdenum films on transparent substrates at low fluences," Appl. Phys. A **102**, 173–178 (2011).
[9]G. Heise, M. Domke, J. Konrad, S. Sarrach, J. Sotrop, and H. P. Huber, "Laser lift-off initiated by direct induced ablation of different metal thin

films with ultra-short laser pulses," J. Phys. D: Appl. Phys. **45**, 315303 (2012).
[10]J.-H. Klein-Wiele and P. Simon, "Sub-100 nm pattern generation by laser direct writing using a confinement layer," Opt. Express **21**, 9017–9023 (2013).
[11]N. C. Anderholm, "Laser-generated stress waves," Appl. Phys. Lett. **16**, 113–115 (1970).
[12]T. Yabe, C. Phipps, M. Yamaguchi, R. Nakagawa, K. Aoki, H. Mine, Y. Ogata, C. Baasandash, M. Nakagawa, E. Fujiwara, K. Yoshida, A. Nishiguchi, and I. Kajiwara, "Microairplane propelled by laser driven exotic target," Appl. Phys. Lett. **80**, 4318–4320 (2002).
[13]J. Sotrop, A. Kersch, M. Domke, G. Heise, and H. P. Huber, "Numerical simulation of ultrafast expansion as the driving mechanism for confined laser ablation with ultra-short laser pulses," Appl. Phys. A **113**, 397–411 (2013).
[14]M. V. Shugaev and N. M. Bulgakova, "Thermodynamic and stress analysis of laser-induced forward transfer of metals," Appl. Phys. A **101**, 103–109 (2010).
[15]S. I. Anisimov, V. V. Zhakhovskii, N. A. Inogamov, K. Nishihara, A. M. Oparin, and Yu. V. Petrov, "Destruction of a solid film under the action of ultrashort laser pulse," JETP Lett. **77**, 606–610 (2003).
[16]A. K. Upadhyay and H. M. Urbassek, "Melting and fragmentation of ultrathin metal films due to ultrafast laser irradiation: a molecular-dynamics study," J. Phys. D: Appl. Phys. **38**, 2933–2941 (2005).
[17]B. J. Demaske, V. V. Zhakhovsky, N. A. Inogamov, and I. I. Oleynik, "Ablation and spallation of gold films irradiated by ultrashort laser pulses," Phys. Rev. B **82**, 064113 (2010).
[18]D. S. Ivanov and L. V. Zhigilei, "Effect of pressure relaxation on the mechanisms of short-pulse laser melting," Phys. Rev. Lett. **91**, 105701 (2003).
[19]Z. Lin and L. V. Zhigilei, "Time-resolved diffraction profiles and atomic dynamics in short-pulse laser-induced structural transformations: Molecular dynamics study," Phys. Rev. B **73**, 184113 (2006).
[20]Z. Lin, E. Leveugle, E. M. Bringa, and L. V. Zhigilei, "Molecular dynamics simulation of laser melting of nanocrystalline Au," J. Phys. Chem. C **114**, 5686–5699 (2010).
[21]E. Leveugle, D. S. Ivanov, and L. V. Zhigilei, "Photomechanical spallation of molecular and metal targets: molecular dynamics study," Appl. Phys. A **79**, 1643–1655 (2004).
[22]L. V. Zhigilei and B. J. Garrison, "Microscopic mechanisms of laser ablation of organic solids in the thermal and stress confinement irradiation regimes," J. Appl. Phys. **88**, 1281–1298 (2000).
[23]C. F. Richardson and P. Clancy, "Picosecond laser processing of copper and gold: A computer simulation study," Mol. Simul. **7**, 335–355 (1991).
[24]C. Cheng and X. Xu, "Mechanisms of decomposition of metal during femtosecond laser ablation," Phys. Rev. B **72**, 165415 (2005).
[25]M. Gill-Comeau and L. J. Lewis, "Ultrashort-pulse laser ablation of nanocrystalline aluminum," Phys. Rev. B **84**, 224110 (2011).
[26]Z. Lin, R. A. Johnson, and L. V. Zhigilei, "Computational study of the generation of crystal defects in a bcc metal target irradiated by short laser pulses," Phys. Rev. B **77**, 214108 (2008).
[27]L. V. Zhigilei, Z. Lin, and D. S. Ivanov, "Atomistic modeling of short pulse laser ablation of metals: Connections between melting, spallation, and phase explosion," J. Phys. Chem. C **113**, 11892–11906 (2009).
[28]E. T. Karim, Z. Lin, and L. V. Zhigilei, "Molecular dynamics study of femtosecond laser interactions with Cr targets," AIP Conf. Proc. **1464**, 280–293 (2012).
[29]C. Wu and L. V. Zhigilei, "Microscopic mechanisms of laser spallation and ablation of metal targets from large-scale molecular dynamics simulations," Appl. Phys. A **114**, 11–32 (2014).
[30]C. Li, J. Zhang, and X. Wang, "Phase change and stress wave in picosecond laser–material interaction with shock wave formation," Appl. Phys. A **112**, 677–687 (2013).
[31]S. I. Anisimov, B. L. Kapeliovich, and T. L. Perel'man, "Electron emission from metal surfaces exposed to ultrashort laser pulses," Sov. Phys. JETP **39**, 375–377 (1974).
[32]D. S. Ivanov and L. V. Zhigilei, "Combined atomistic–continuum modeling of short-pulse laser melting and disintegration of metal films," Phys. Rev. B **68**, 064114 (2003).
[33]S. M. Foiles, M. I. Baskes, and M. S. Daw, "Embedded-atom-method functions for the fcc metals Cu, Ag, Au, Ni, Pd, Pt, and their alloys," Phys. Rev. B **33**, 7983–7991 (1986).
[34]A. F. Voter and S. P. Chen, "Accurate interatomic potentials for Ni, Al, and Ni_3Al," Mater. Res. Soc. Symp. Proc. **82**, 175–180 (1987).
[35]C. Wu, D. A. Thomas, Z. Lin, and L. V. Zhigilei, "Runaway lattice-mismatched interface in an atomistic simulation of femtosecond laser irradiation of Ag film—Cu substrate system," Appl. Phys. A **104**, 781–792 (2011).
[36]*Handbook of Chemistry and Physics*, edited by R. C. Weast, 64th ed. (CRC Press, Boca Raton, 1983).
[37]E. Leveugle and L. V. Zhigilei, "Molecular dynamics simulation study of the ejection and transport of polymer molecules in matrix-assisted pulsed laser evaporation," J. Appl. Phys. **102**, 074914 (2007).
[38]B. J. Garrison, T. E. Itina, and L. V. Zhigilei, "Limit of overheating and the threshold behavior in laser ablation," Phys. Rev. E **68**, 041501 (2003).
[39]A. Miotello and R. Kelly, "Laser-induced phase explosion: new physical problems when a condensed phase approaches the thermodynamic critical temperature," Appl. Phys. A **69**, S67–S73 (1999).
[40]N. M. Bulgakova and A. V. Bulgakov, "Pulsed laser ablation of solids: transition from normal vaporization to phase explosion," Appl. Phys. A **73**, 199–208 (2001).
[41]R. W. Ohse and H. von Tippelskirch, "The critical constants of the elements and of some refractory materials with high critical temperatures. (A review)," High Temp.-High Press. **9**, 367–385 (1977).
[42]Z. Lin, L. V. Zhigilei, and V. Celli, "Electron-phonon coupling and electron heat capacity of metals under conditions of strong electron-phonon nonequilibrium," Phys. Rev. B **77**, 075133 (2008).
[43]D. Bäuerle, *Laser Processing and Chemistry* (Springer-Verlag, Berlin, 2000).
[44]N. W. Ashcroft and N. D. Mermin, *Solid State Physics* (Holt, Rinehart and Winston, New York, 1976).
[45]L. V. Zhigilei and B. J. Garrison, "Pressure waves in microscopic simulations of laser ablation," Mater. Res. Soc. Symp. Proc. **538**, 491–496 (1999).
[46]C. Schäfer, H. M. Urbassek, L. V. Zhigilei, and B. J. Garrison, "Pressure-transmitting boundary conditions for molecular-dynamics simulations," Comput. Mater. Sci. **24**, 421–429 (2002).
[47]K. S. Gadre and T. L. Alford, "Contact angle measurements for adhesion energy evaluation of silver and copper films on parylene-n and SiO_2 substrates," J. Appl. Phys. **93**, 919–923 (2003).
[48]A. Vogel and V. Venugopalan, "Mechanisms of pulsed laser ablation of biological tissues," Chem. Rev. **103**, 577–644 (2003).
[49]G. Paltauf and P. E. Dyer, "Photomechanical processes and effects in ablation," Chem. Rev. **103**, 487–518 (2003).
[50]L. V. Zhigilei, Z. Lin, D. S. Ivanov, E. Leveugle, W. H. Duff, D. Thomas, C. Sevilla, and S. J. Guy, "Atomic/molecular-level simulations of laser-materials interactions," in *Laser-Surface Interactions for New Materials Production: Tailoring Structure and Properties*, Springer Series in Materials Science Vol. 130, edited by A. Miotello and P. M. Ossi (Springer Verlag, New York, 2010), Chap. 3, pp. 43–79.